Article:
Langran-Wheeler, C., Rigby, S. orcid.org/0000-0001-6844-3797, Clarke, S.D. orcid.org/0000-0003-0305-0903 et al. (3 more authors) (2021) Near-field spatial and temporal blast pressure distributions from non-spherical charges: Horizontally-aligned cylinders. International Journal of Protective Structures, 12 (4). pp. 492-516. ISSN 2041-4196

https://doi.org/10.1177/20414196211013443

Research Article

International Journal of
Protective Structures

Near-field spatial and temporal blast pressure distributions from non-spherical charges: Horizontally-aligned cylinders

International Journal of Protective Structures
1–25

DOI: 10.1177/20414196211013443
journals.sagepub.com/home/prs


Christian Langran-Wheeler[1], Sam Rigby[1], Sam David Clarke[1], Andy Tyas[1,2], Catie Stephens[3] and Robert Walker[3]

Abstract

Research into the characterisation of blast loading on structures following the detonation of a high explosive commonly assumes that the charge is spherical. This has the advantage of simplifying experimental, analytical and computational studies. In practice, however, designers of protective structures must often consider explosive threats which have other geometric forms, which has significant influence on the loading imparted to structures very close to the explosion source. Hitherto, there has been little definitive experimental investigation of the 'near-field' blast load parameters from non-spherical explosive charges and studies that have been conducted are usually confined to measurement of the total impulse imparted to a target. Currently, a detailed understanding of the development of loading on a target, necessary to fully inform the design process and appraise the efficacy of predictions from computational models, is lacking. This article, the first part of a wider investigation into these geometrical effects, details work conducted to address this deficiency. Results are presented from an experimental study of loading from detonations of cylindrical charges, set with the longitudinal axis parallel to an effectively rigid target, instrumented to facilitate the capture of the spatial and temporal evolution of the loading at different radial and angular offsets from the charge. These results are compared against loads from spherical charges and the effect of charge shape is identified. Significant differences are observed in the mechanisms and magnitude of loading from cylindrical and spherical charges, which is confirmed through the use of numerical analysis. The overall study provides insights which will assist the future design of effective protection systems.

Keywords

Blast load, cylindrical explosive, experiment, Hopkinson pressure bar, pressure, specific impulse

[1]Department of Civil and Structural Engineering, University of Sheffield, Sheffield, UK
[2]Blastech Ltd., The BioIncubator, Sheffield, UK
[3]US Army Engineer Research and Development Center (ERDC), Geotechnical and Structures Laboratory, Vicksburg, MS, USA

Corresponding author:
Sam Rigby, Department of Civil and Structural Engineering, University of Sheffield, Mappin Street, Sheffield, S1 3JD, UK.
Email: sam.rigby@shef.ac.uk

Introduction

The loading imparted to a structure following detonation of a non-spherical high explosive may differ significantly from that of a spherical charge. This difference is particularly pronounced in the near-field, which is characterised by extremely high magnitude, highly non-uniform (spatial and temporal) loading (Rigby et al., 2015b) and interaction of the detonation product cloud with the target surface (Tyas et al., 2016). Loading from spherical charges has been the subject of considerable research efforts for many decades, and there are relatively well-established tools for predicting the magnitude and distribution of loading from spherical airbursts or hemispherical surface bursts, for example, the Kingery and Bulmash (1984) semi-empirical predictions that form the basis of the UFC 3-340-02 manual (US Department of Defence, 2008) and ConWep (Hyde, 1991). However, characterisation of blast loading from even the simplest non-spherical charges has received significantly less attention, despite their prevalence in real-world events.

Detonation of a cylindrical explosive results in the generation of two forms of shock wave: one set emitted from each end of the cylinder, and one emanating out radially from the curved surface of the charge (Wisotski and Snyer, 1965). The two sets of waves travel perpendicular to each other; the ends of the primary waves interact at an oblique angle (relative to the axis of the charge) generating bridging waves and a Mach Stem where the waves meet. Secondary waves are created as the Mach reflections travel inwards from the Mach Stems, facilitating a transfer of energy from the direction of the greater primary shock wave to the lesser. This is shown schematically in Figure 1, with charge dimension and measurement locations used in this study also shown. The relative energy propagating in each primary wave is dependent on the aspect ratio of the cylinder, that is, the ratio between the length (or height) of the charge and its diameter: L/D.

Stoner and Bleakney (1948) analysed the data from 56 experimental trials to establish free-air incident pressure-distance relations from rectangular charges (17 tests using TNT), spherical charges (eight tests using Pentolite) and cylindrical charges (31 tests: 5 Pentolite and 26 TNT). Pressure was not directly measured, rather it was inferred from the velocity-radius data compiled from various time-of-arrival piezo-electric gauges. Whilst a number of different L/D ratios were considered (ranging from 1.32 to 5.20), the authors remarked that there were insufficient tests to analyse the data with statistical significance. However, the results showed a dependence on L/D, and a clear difference between the spherical and cylindrical pressure-distance was observed, with the radial shock wave remaining near-cylindrical in the near-field with a slower decay than a spherical shock wave and therefore relatively higher pressures in that range. Pronounced differences between spherical and cylindrical pressures were continued to be observed at distances greater than 20 charge diameters (approximately $Z > 1.8$ m/kg$^{1/3}$: the closest measurement locations in the trials), with the $L/D = 5.20$ charges exhibiting pressures that were an average of 10% higher than the spherical charges out to a scaled distance of approximately $Z = 3.0$ m/kg$^{1/3}$.

Plooster (1978) used experimental data available at the time to derive incident pressure-distance relationships for cylinders of varying L/D. This work was later developed with the inclusion of new experimental data using 3.6 and 7.2 kg Pentolite charges (Plooster, 1982), incorporating a wider range of L/D ratios (0.25–6.00). The complexities of the emergent blast wave profile from cylindrical charges, in contrast to the spherically-symmetric nature of blast waves from spherical explosives, resulted in a clear dependency of blast loading on azimuth angle, defined as the angle between the longitudinal axis of the cylinder and the measurement axis (Esparza, 1992). Localised variations in blast loading were observed as a function of both azimuth angle and orientation of the long axis of the cylinder to the measurement location. Experimental data were available for $Z > 1.24$ m/kg$^{1/3}$. Further, Hopkinson-Cranz scaling (Cranz, 1926; Hopkinson, 1915) has been shown to be applicable for cylindrical charges in the far-field (Swizdak, 1982).

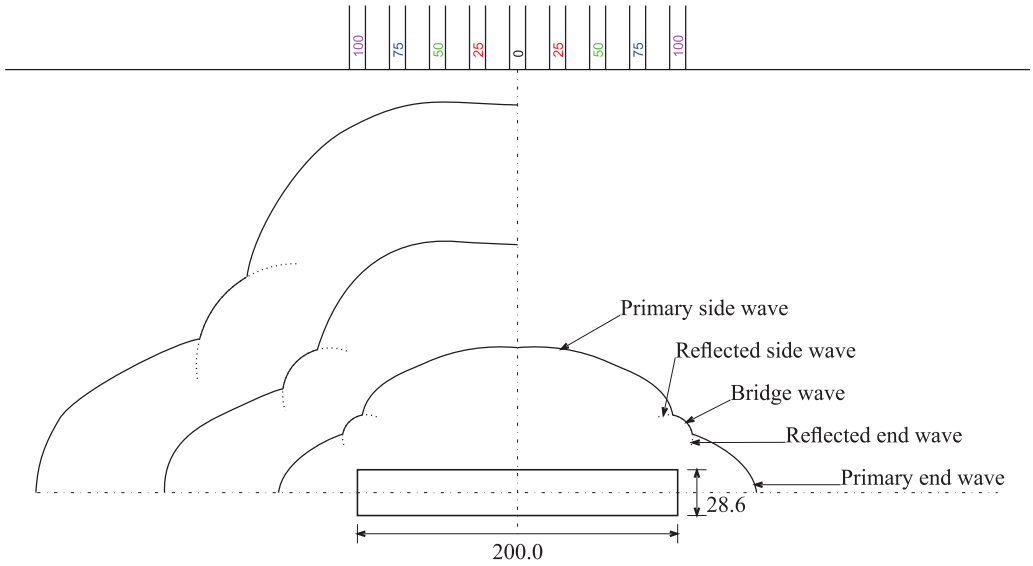

Figure 1. Primary and secondary shock waves emanating from a cylindrical explosive, adapted from Wisotski and Snyer (1965). Also shown are dimensions of a $L/D = 7$ cylinder and measurement locations used in this study (in mm). Numbers at each measurement location denote distance from the centre of the target.

The propagation of blast waves from cylindrical charges and their dependency on aspect ratio and scaled distance has been the subject of recent experimental and numerical investigations. Wu et al. (2010) studied the effect of L/D, charge orientation, and scaled distance on blast parameters from cylindrical charges using finite element analysis, supplemented by a small number of experiments, and observed that peak reflected pressure and impulse from a vertically-orientated cylinder (axis perpendicular to the span of the target) were much larger than those from a spherical charge of equal mass, or a horizontally-orientated cylinder. Similar findings are reported in the work of Sherkar et al. (2016), Artero-Guerrero et al. (2017) and Langran-Wheeler et al. (2017, 2019), and it is well-reported that for large values of L/D the majority of energy is focused in the radial direction, whereas for small values of L/D the majority of energy is focused in the axial direction. Rigby et al. (2019b) experimentally measured near-field specific impulse distributions from spheres and $L/D = 1/3$ cylindrical charges and observed that the cylindrical charges imparted a similar total impulse to the spherical charges of equal mass, despite being placed three times greater distance from the target.

Knock and Davies (2011a, 2011b, 2013) and Knock et al. (2015) developed empirical equations to predict incident blast parameters emanating from the axial and radial directions of a cylindrical explosive. Simoens and Lefebvre (2015) experimentally measured mid- to far-field (0.5–2.5 m/kg $^{1/3}$) incident blast pressures from cylindrical charges and derived spherical equivalence factors (the mass of spherical explosive required to impart the same load as a unit-mass of cylindrical explosive) ranging from 0.8 to 1.8 for incident pressure and 0.6–1.4 for incident specific impulse. Recently, spherical equivalence factors have been derived for a range of cylindrical charges ($L/D = 0.2$–5.0) by equating plate deformations using finite element analysis (Rigby et al., 2021). Cylindrical blast parameters have also been shown to be dependent on initiation location and recent studies have shown that pressure can be enhanced by up to a factor of 3.0 for centrally-detonated cylinders (Hu et al., 2018; Xiao et al., 2020a, 2020b).

It is generally accepted that differences between cylindrical and spherical blast parameters persist to a distance of $Z \approx 4$ m/kg $^{1/3}$ (Sherkar et al., 2016; Simoens and Lefebvre, 2015; Xiao et al., 2020b), however there is currently a lack of robust understanding of the early and mid stages of blast wave propagation following detonation of a non-spherical charge. This stems from a dearth of experimental data or studies of near-field blast loading, with very few studies reporting experimental results for non-spherical charges at scaled distances less than 1.24 m/kg $^{1/3}$ (Shi and Stewart, 2015). The objective of this work is to develop a better understanding of non-spherical charges, specifically long cylinders, through experimental studies and numerical modelling. This paper presents the experimental results from a series of tests measuring the spatial and temporal distribution of reflected blast pressures following detonation of 200 g horizontally-orientated (longitudinal axis parallel to target span) cylindrical C4 charges ($L / D = 7$) in free air, $Z = 0.452$ m/kg $^{1/3}$. Blast pressure distributions are compared to those from spherical charges with equal mass in order to make direct observations on the influence of charge geometry and orientation on the blast load developed on the surface of a rigid target. Indicative numerical modelling is used to further investigate and qualify these observations. Finally, discrete pressure measurements are integrated spatially and temporally to quantify total impulse acting on the instrumented area. The results show a clear difference in the form and magnitude of loading imparted to a target following detonation of a cylindrical explosive: the loading is less uniform and less repeatable across the target face, and higher in magnitude by approximately a factor of two.

Experimental work

Preliminary far-field testing

All experimental work reported in this article was conducted at the The University of Sheffield Blast and Impact Laboratory in Buxton, UK. Three preliminary arena tests were performed, following the methodology outlined in Rigby et al. (2015a). Far-field reflected pressure histories were recorded following detonation of 312.5 g hemispheres of Composition 4 (C4) bare HE charges. The aim of this initial study was to characterise the C4 explosive and to demonstrate consistency of far-field test parameters, such that any variations in loading observed in subsequent near-field testing could be attributed to genuine physical features rather than experimental error.

Reflected pressure was measured using a single Kulite HKM-375 7 bar pressure transducer, mounted at ground level, flush with the exterior of a 500 mm thick blockwork-covered reinforced concrete bunker wall. The bunker wall was 4.5 m high and extended more than 10 m horizontally from the measurement location, ensuring that no clearing waves would reach the gauge location during the loading duration (Tyas et al., 2011). Data were recorded using Tie-Pie HAS Handyscope USB digital oscilloscopes at 14-bit resolution at a sampling rate of 1.562 MHz, which were triggered via a low-voltage breakwire embedded with the detonator. Three tests were conducted in total, with the charges placed at 2, 4 and 6 m stand-off distances. The explosives were sat on a small steel anvil to prevent repeat damage to the concrete ground slab, and were centrally-detonated using Nitronel MS 25 non-electronic shock-tube detonators.

Figure 2 shows the pressure and specific impulse histories (determined through cumulative numerical integration of the pressure signals with respect to time) for each of the three tests. Also shown are the UFC 3-340-02 (US Department of Defence, 2008) semi-empirical predictions, with the negative phase constructed using the relationships presented in Rigby et al. (2014a), assuming a TNT equivalence of 1.20 (Bogosian et al., 2016). Note that the 2 and 6 m experimental timebases were adjusted by 0.1 ms to better align with the semi-empirical predictions for clarity of presentation.

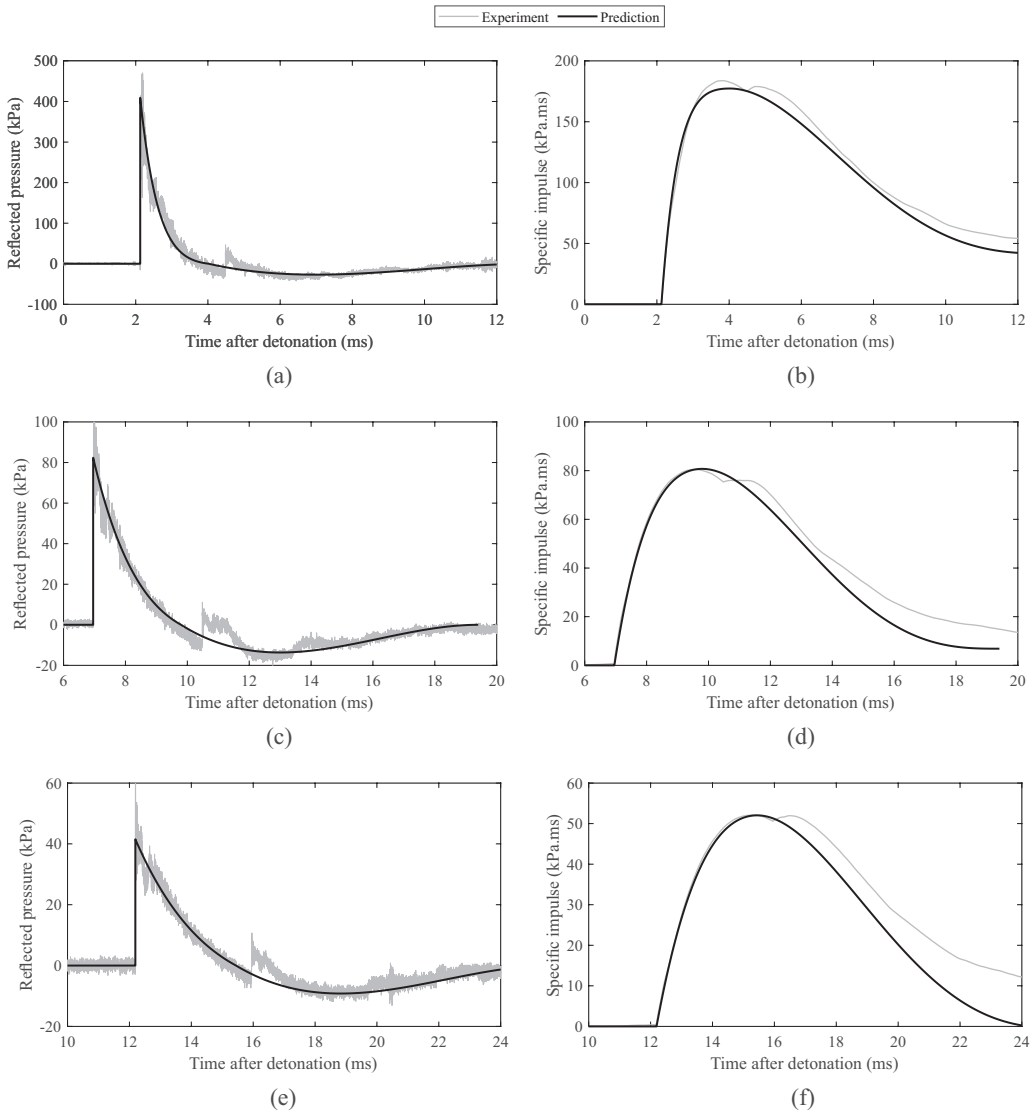

Figure 2. Compiled far-field pressure and impulse histories and semi-empirical predictions for 312.5 g hemispheres of C4: (a–b) 2 m stand-off, (c–d) 4 m stand-off, and (e–f) 6 m stand-off.

Generally the results appear in excellent agreement, especially prior to the arrival of the secondary shock shortly after the start of the negative phase (Rigby and Gitterman, 2016). Thereafter the results begin to diverge slightly on account of the secondary shock not being accounted for in the predictions. Experimental and semi-empirical positive phase blast parameters are summarised in Table 1. Here, experimental peak pressure values were determined by fitting a modified Friedlander (1946) exponential decay to the recorded pressure history, after removing the first 25% of the positive phase to negate the effects of sensor ringing and any electrical noise that may have been recorded and extrapolating back to the arrival time (Rigby et al., 2014c). It can be seen that the predicted values are accurate to within $\pm$ 5% throughout, which gives confidence that a high level of experimental control has been achieved.

Table 1. Summary of far-field test results and semi-empirical predictions for 312.5 g hemispheres of C4.

Test no.	Stand-off (m)	Peak reflected pressure (kPa)			Peak specific impulse (kPa.ms)		
		Experiment	Prediction	% diff.	Experiment	Prediction	% diff.
1	2	418.0	409.1	2.1	183.8	177.3	3.6
2	4	86.5	82.4	4.8	80.5	80.7	0.3
3	6	42.6	41.5	2.6	52.1	52.0	0.2

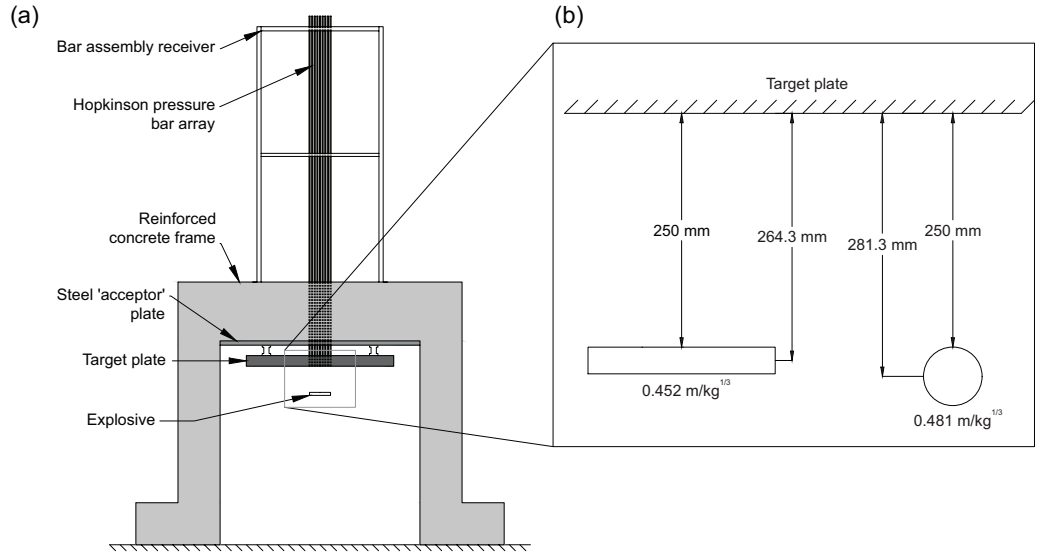

Figure 3. Schematic of the *Characterisation of Blast Loading* apparatus: (a) general arrangement, after Clarke et al. (2015) and (b) definition of stand-off and scaled distances used in this study (left: cylinders, right: spheres).

Near-field apparatus and data acquisition

Near-field tests were performed using the *Characterisation of Blast Loading* (CoBL) apparatus (Clarke et al., 2015), shown in Figure 3; originally designed to measure the output from buried explosives but since used to quantify near-field reflected blast pressures from free-air explosions (Rigby et al., 2015b, 2019b, 2020; Tyas et al., 2016).

The apparatus, as utlisied for this study, comprises an array of 17 Hopkinson (1914) pressure bars 152 (HPBs), suspended vertically such that their faces lie flush with the surface of a 100 mm thick, 1400 mm diameter high-strength steel plate that acts as a nominally rigid reflecting surface, under which the explosives are detonated. The target plate is underslung from the soffits of a pair of steel fibre and bar reinforced concrete A-frames, located approximately 1 m apart, via a 50 mm thick steel 'acceptor' plate cast into the frame to enable the target plate to be affixed. Each A-frame comprises two 500 mm square columns with a 750 mm deep, 500 mm wide concrete beam spanning between the two columns.

The 3.25 m long, 10 mm diameter EN24(T) steel HPBs are formed into two perpendicular arrays of nine bars (with a common central bar: 17 bars in total) that form a cross, centred on the centre

Table 2. Summary of near-field test arrangements used in this study.

Test nos.	Shape	Orientation	Stand-off (m)	
			Clear	To centre
4–5	Sphere	n/a	0.250	0.281
6–8	Cylinder	Aligned	0.250	0.264
9–10	Cylinder	45°	0.250	0.264

of the target plate. The distal ends of the bars are threaded to permit fine adjustments to their height at the bar assembly receiver. The bars are located at 25 mm centres, thereby providing a 200 mm diameter instrumented region in the centre of the target plate. Spatial and temporal pressure distributions are recorded at each bar location using pairs of perimeter-mounted Kyowa KSP-2-120-E4 semi-conductor strain gauges in a Wheatstone bridge circuit to neglect any bending in the bars. The strain gauges are located 250 mm from the loaded face of each bar and record axial stress history up to ~ 1.2 ms from arrival of the stress pulse at the gauge location (Clarke et al., 2015), subjected to a theoretical bandwidth of ~ 250 kHz (Tyas and Watson, 2001).

As with the far-field tests, data were recorded using Tie-Pie HAS Handyscope USB digital oscilloscopes at 14-bit resolution with the sampling rate increased to 3.125 MHz. Again, recording was triggered via a low voltage break-wire wrapped around the detonator. Recorded signals are converted to stress by zeroing against the pre-trigger voltage and applying a known calibration factor. Occasionally strain gauges de-laminate from the surface of the bars creating erroneous or nil traces, which are identified and removed from the dataset.

Time of detonation was established by scrutinising the break-wire trace for the first sign of voltage change prior to triggering, which in addition to the time taken for the stress pulse to reach the gauge location from the face of the HPB (50 μs), was subtracted from the timebase of the pressure signals in post-processing. No rcadditional post-processing, for example, smoothing, frequency filters and dispersion correction, is applied to the signals, although pressure traces in this article are presented as test- or series-averaged to aid in qualitative discussion.

Near-field test arrangement

Seven near-field tests were performed in total: two tests using 200 g spheres of C4 (31.3 mm radius) and five tests using 200 g C4 cylinders (200.0 mm long, 14.3 mm radius, $L / D = 7$); see Table 2. Of the five cylindrical charge tests, three tests were performed with the longitudinal axis of the charge aligned directly with one of the HPB arrays, and two tests were performed with the longitudinal axis of the charge set at 45° to the HPB arrays in order to study the effects of charge alignment; see Figure 4. The charges were detonated at a clear stand-off distance of 250 mm. Although this gives slightly different values of scaled distance (to charge centre, 0.452 and 0.481 m/kg $^{1/3}$ for the cylindrical and spherical charges respectively) on account of the different cylindrical and spherical charge radii, a consistent clear stand-off facilitates comparison with blast pressure measurements from vertically aligned cylinders, which forms part of a later study.

The C4 bare charges were shaped using bespoke 3D printed charge moulds. The charges were suspended on an ultra-light (25 g/m^2) woven glass fibre fabric pulled taught within a steel ring; see Figure 5. The ring was placed on adjustable legs allowing the charge to be levelled (with respect to the target plate) and precisely located beneath the centre of the target plate. Two perpendicular laser

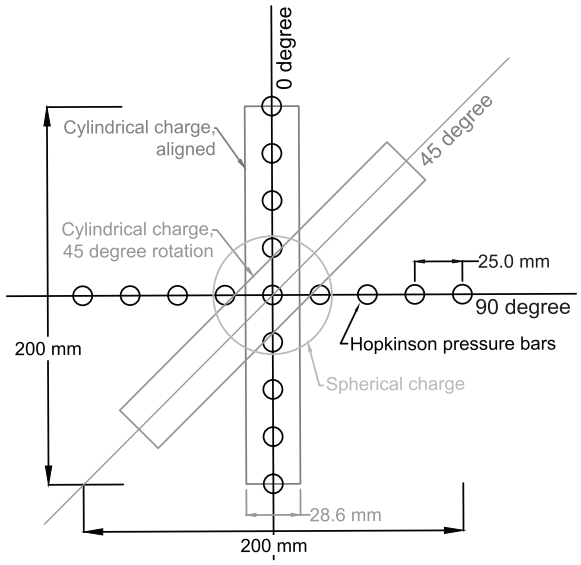

Figure 4. Plan view of the instrumented area indicating HPB layout and charge orientation used in the spherical, aligned cylindrical and 45° cylindrical tests (to scale).

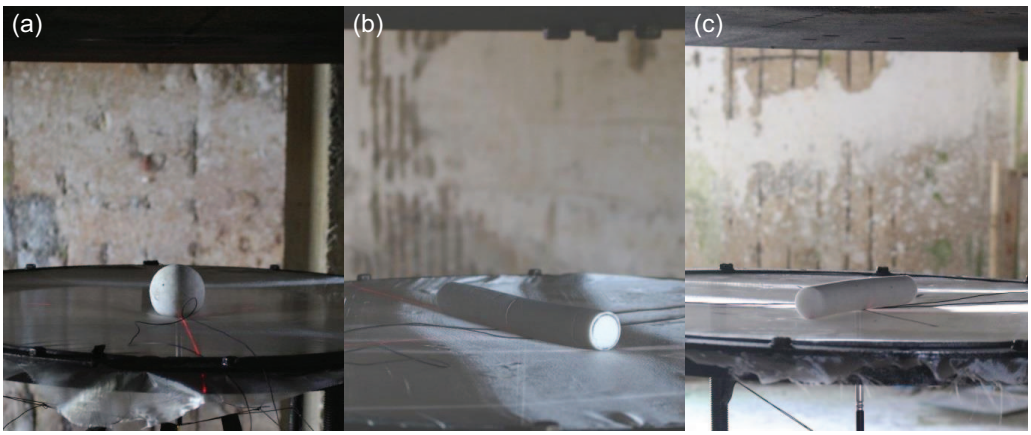

Figure 5. Photographs of experimental setup, charge support and alignment: (a) sphere, (b) aligned cylinder and (c) 45° cylinder.

levels were used to ensure the cylindrical charges were aligned correctly. All charges were surface-detonated using Nitronel MS 25 non-electronic shock-tube detonators placed in-line with the centre of the charge from beneath, to support the charge prior to testing and to minimise sagging of the glass fibre fabric support. Inserting the detonator into the explosive would have compromised the structure of the charge during forming and handling, and previous experimental work has shown that locating the detonator between the charge and the target introduces a high degree of electrical noise (Fay et al., 2013).

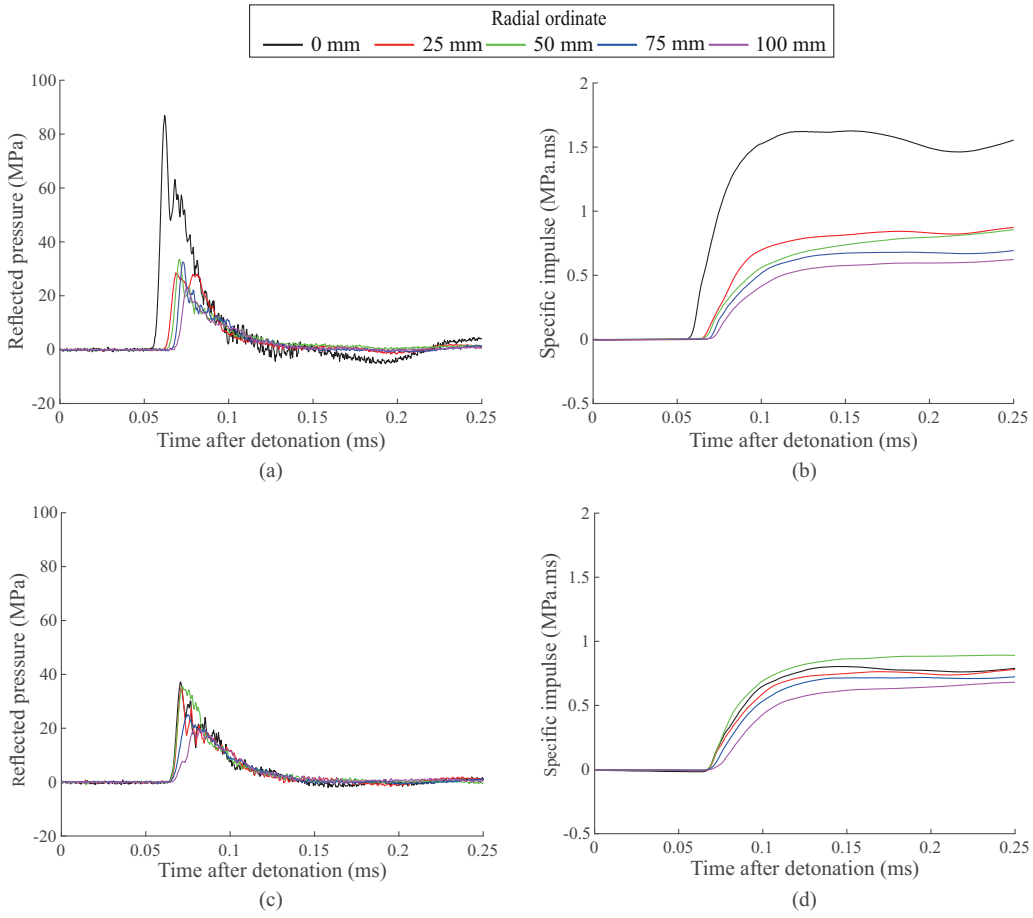

Figure 6. Test-averaged reflected pressure and specific impulse histories from detonation of 200 g spheres of C4 at 250 mm clear stand-off: (a–b) Test 4 and (c–d) Test 5.

Results

Spherical tests

Reflected pressure and specific impulse histories from the spherical charge tests are shown in Figure 6. In order to facilitate a qualitative comparison between the tests, traces at 25–100 mm are presented as the test-average of the pressure and impulse histories recorded by the four bars at each radial ordinate, and the '0 mm' bar shows the single central bar pressure trace in each test. Averaging the pressure signals for each of the non-central HPB locations in this manner allows for general features of the loading, which otherwise may be indistinguishable when viewing the trace from a single bar, to be observed. This is also an effective way to reduce the effect of signal noise and electrical spikes without the need for a smoothing algorithm, and maintains the primary physical features of the applied loading. Averaging was achieved by aligning the central bar such that the time each pressure signal had risen to one-third its peak value was coincident across the tests in question. All other pressure traces were shifted by the same time to maintain variations in arrival

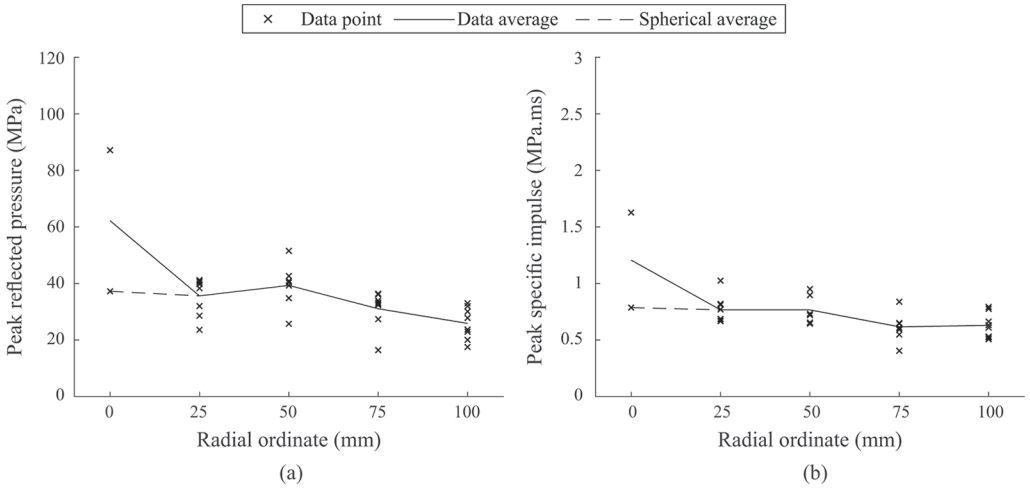

Figure 7. Compiled peak reflected pressure (a) and peak specific impulse (b) versus radial ordinate from detonation of 200 g spheres of C4 at 250 mm clear stand-off.

time with distance from the plate centre. In no case was it necessary to adjust each signal by more than 6.73 μs.

The reflected pressure traces appear to resemble a typical Friedlander-type decay, characterised by a clear rise to peak pressure and relatively consistent (for all radial ordinates) decay to ambient pressure. The loading appears to be spatially near-uniform at a given time after arrival of the wave at the most remote measurement location. The traces exhibit features of Pochhammer-Chree dispersion (Rigby et al., 2018a), that is, degradation of the transient pressure features with durations less than 5 μs and spurious oscillations in the pressure traces as a result of the wave propagating through a finite diameter bar over a distance to the location of the strain gauge. The general form of the pressure pulse and the temporal development of specific impulse are largely unaffected by dispersion.

Whilst the recorded pressure histories at 25–100 mm appear highly consistent, there is evidence of localised variability in the blast loading at the central bar. It has been suggested that $Z \approx 0.5\,\mathrm{m/kg}^{1/3}$ marks the transition between '*relatively consistent [loading]*' in the extreme near-field and '*large variations in loading*' in the late near-field (Tyas, 2019). The results in Figure 6 ($Z = 0.481\,\mathrm{m/kg}^{1/3}$) lend evidence to this claim; it appears as though a turbulent fireball plume – likely caused by the emergence and growth of Rayleigh-Taylor (Lord Rayleigh, 1882; Taylor, 1950) and Richtmyer-Meshkov (Meshkov, 1969; Richtmyer, 1960) surface instabilities (Rigby et al., 2020) – has impacted the central bar in Test 4 and not in Test 5. Whilst the central bar loading in Test 5 appears to be commensurate with the other radial ordinates, the central bar loading in Test 4 demonstrates an earlier arrival time, higher magnitude peak pressure and generally higher pressure-time history thereafter.

Figure 7 shows compiled peak reflected pressure (a), and peak specific impulse (b) versus radial ordinate for the spherical charge tests (Test 4 and Test 5). Note that the results shown here are for each HPB, rather than the test-averaged values discussed previously. For 25–100 mm radial ordinates the peak pressures and specific impulses can be seen to form a reasonably tight banding around the mean values (solid line), with the results typically within $\pm$ 10 MPa and $\pm$ 0.25 MPa.ms of the mean peak pressure and peak specific impulse, respectively, at each radial ordinate. Conversely, the effect of fireball plume impingement on the central bar in Test 4, as discussed

previously with reference to Figure 6, can be clearly seen. In order to provide a fair baseline to compare the spherical loading distributions to subsequent tests using cylindrical charges, the central bar data from Test 4 has been omitted when calculating the average distributions (as indicated by the dashed line in Figure 7). At this scaled distance, the peak loading is relatively uniform across the central 200 mm diameter of the target plate.

Cylindrical tests

Of the five cylindrical charge experiments, three were performed with the longitudinal axis of the charge located directly beneath the centreline of one of the HPB arrays, as in Figure 4. This generates two subsets of HPB data for each of these tests, corresponding to the HPB arrays aligned 'parallel' with, and 'perpendicular' to, the longitudinal axis of the charge, denoted by the 0° and 90° arrays respectively in Figure 4. For the two tests where the cylinders were aligned at 45° to the HPB arrays, each measurement location is symmetric about the longitudinal axis of the charge. This generates a single dataset from which mean values can be taken at each radial ordinate using all four HPB measurements (with the exception of the central bar), as with the spherical data. Collectively, this enables blast loading distributions to be evaluated separately at radial ordinates along arrays orientated at 0°, 45° and 90° to the longitudinal axis of the charge.

Figure 8 presents the series-averaged pressure and impulse histories of the aligned tests (Tests 6–8) and the 45° tests (Tests 9 and 10). Here, the presented pressure traces are taken as the average at each HPB location for all tests within the series, again to aid in clarity of presentation and to allow comments to be made on the general behaviour and temporal form of the loading. The data from Tests 6 to 8 are separated into the parallel and perpendicular components (two HPB arrays in each subset per test), as indicated by the small illustration in each sub-figure indicating the HPB array from which the data are taken.

The reflected pressure histories in Figure 8 appear more complex and higher in magnitude than the corresponding spherical pressure histories (Figure 6). The traces bear less resemblance to the Friedlander-type exponential decays observed in the spherical charge tests: peak pressure is often reached some time after first arrival of the shock front, with a more irregular decay and longer positive phase duration (relative to the spherical loading) exhibited thereafter. This results in a consistently higher specific impulse at all radial ordinates compared to the spherical charges.

As expected, the arrival times of the shock are broadly similar at each radial offset in the 0° case and increase with radial offset in the 90° case. The pressure traces at the 50 and 75 mm bar locations at 0° orientation are approximately twice those at the same bar locations for 90° orientation, with the 45° results approximately halfway between the two for all radial ordinates except the central bar (which is common to both 0° and 90° arrays).

At 0° orientation the highest peak pressures are off-centred, with the 50 and 75 mm bars recording an average peak pressure higher than that recorded by the central bar. These larger non-central pressures persist until approximately 0.08 ms, after which the non-central bars (in particular those at 75 and 100 mm from the centre) record a rapid temporal decay in pressure. This may be attributed to localised 'clearing' or equalisation of pressures in the regions outside of the projected area of the charge.

The temporal development of specific impulse at the central bar is initially more gradual but eventually surpasses the specific impulse at the 50 and 75 mm bars due to prolonged high pressure between 0.10 and 0.15 ms which is not present at other locations. This general behaviour is also seen at 45° orientation, however the 50 and 75 mm bars record a less significant pressure increase above the central bar than for the same bars at 0° orientation. With the exception of the 25 mm bar, the peak specific impulse decreases with increasing distance from the plate centre, with the 100 mm

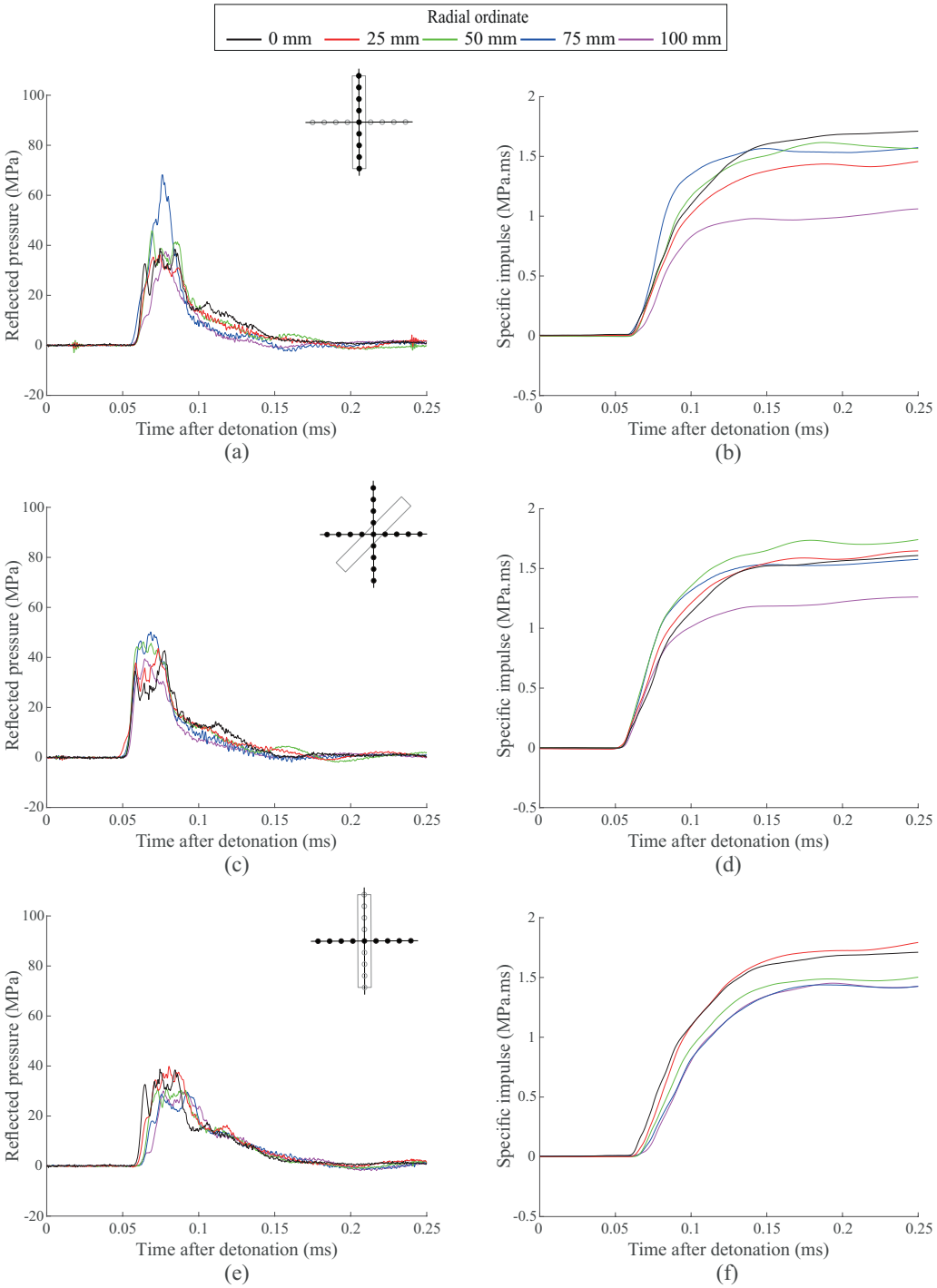

Figure 8. Series-averaged reflected pressure and specific impulse histories from detonation of 200 g $L/D = 7$ cylinders of C4 at 250 mm clear stand-off: (a–b) 0°, (c–d) 45° and (e–f) 90°.

bar recording an impulse that is approximately 30% lower than the remaining bars. In the 0° orientation tests, the 100 mm bars align exactly with each end of the charge, suggesting that this location marks the transition between highly concentrated loading immediately above the charge, to a more low-level loading outside of this region, hence the presence of localised clearing driven by pressure equalisation between these two regions.

Peak specific impulse at the 100 mm bar location and 90° orientation does not exhibit such behaviour, suggesting that this is indeed an effect that originates at the end of the cylindrical charge. From 0.1 ms onwards the pressure traces at 90° orientation appear relatively consistent, with the peak specific impulses slightly decreasing with distance from the plate centre, in line with the delayed arrival times. Since the 0° and 90° arrays are subsets from the same two tests, the central bar traces are common between Figure 8(a) and (e). The prolonged high pressure recorded by the central bar between 0.10 and 0.15 ms, relative to the remaining bars at 0° orientation, appears to match the pressure loading in the remaining bars at 90°, suggesting that this elongated pressure pulse is characteristic of the loading acting perpendicular to the longitudinal axis of the charge. Thus, the parallel component of loading is characterised by uniform arrival times, a sharp rise to peak pressure and more rapid decay to ambient pressure, with a sharp drop-off in loading beyond the ends of the cylinder. Conversely, the perpendicular component of loading is characterised by staggered arrival times, a more gradual rise to peak pressure and a prolonged decay to ambient pressure thereafter. Loading at 45° appears to be a hybrid of these two types of loading.

Discussion

Comparison with spherical data

Figure 9 shows the peak reflected pressures and peak specific impulse distributions from all cylinder orientations. In each plot the solid black line shows how the mean recorded values vary with radial ordinate, with the dashed black line showing the spherical mean distributions from Figure 7 with central bar data from Test 4 omitted. It should be noted that the values here represent the peak value recorded at *any time* for a given bar, which will be different to the maximum values determined from the test-averaged or series-averaged traces in Figures 6 and 8 since these are based solely on the time at which the average pressure across all like bars is highest. Mean distributions are compiled in Table 3. As introduced previously, HPB data is well known to exhibit frequency-dependent dispersion, modifying the pressure profile such that the recorded pressure deviates from the true reflected pressure experienced at the face of the bar. This makes establishing a definitive peak pressure difficult but does not diminish the comparative value of the data. Dispersion does not affect the recording of peak specific impulse, which is a key parameter in assessing structural deformation to blast loads (Rigby et al., 2019a), and therefore recorded specific impulse distributions are highly indicative of the true specific impulse acting on the target face.

The cylindrical peak pressure at the target centre (invariant of orientation angle since the cylinders are rotated about this point) is approximately equal to the epicentral peak pressure from the spherical charge, however the corresponding specific impulse value is approximately twice that from the spherical charge. At 0° and 45° the maximum pressure is clearly non-central (at 75 mm in both cases). This is also observed in the specific impulse distributions for these two orientations, albeit to a lesser extent, which both demonstrate a higher specific impulse at 50 mm than the epicentral value. It is suggested that this behaviour is due to the complex interactions between the target plate and the coalescence of the primary waves from the radial (‘side’) and axial faces (‘end’) of the charge and the bridging wave between the two. This is investigated further in the following section.

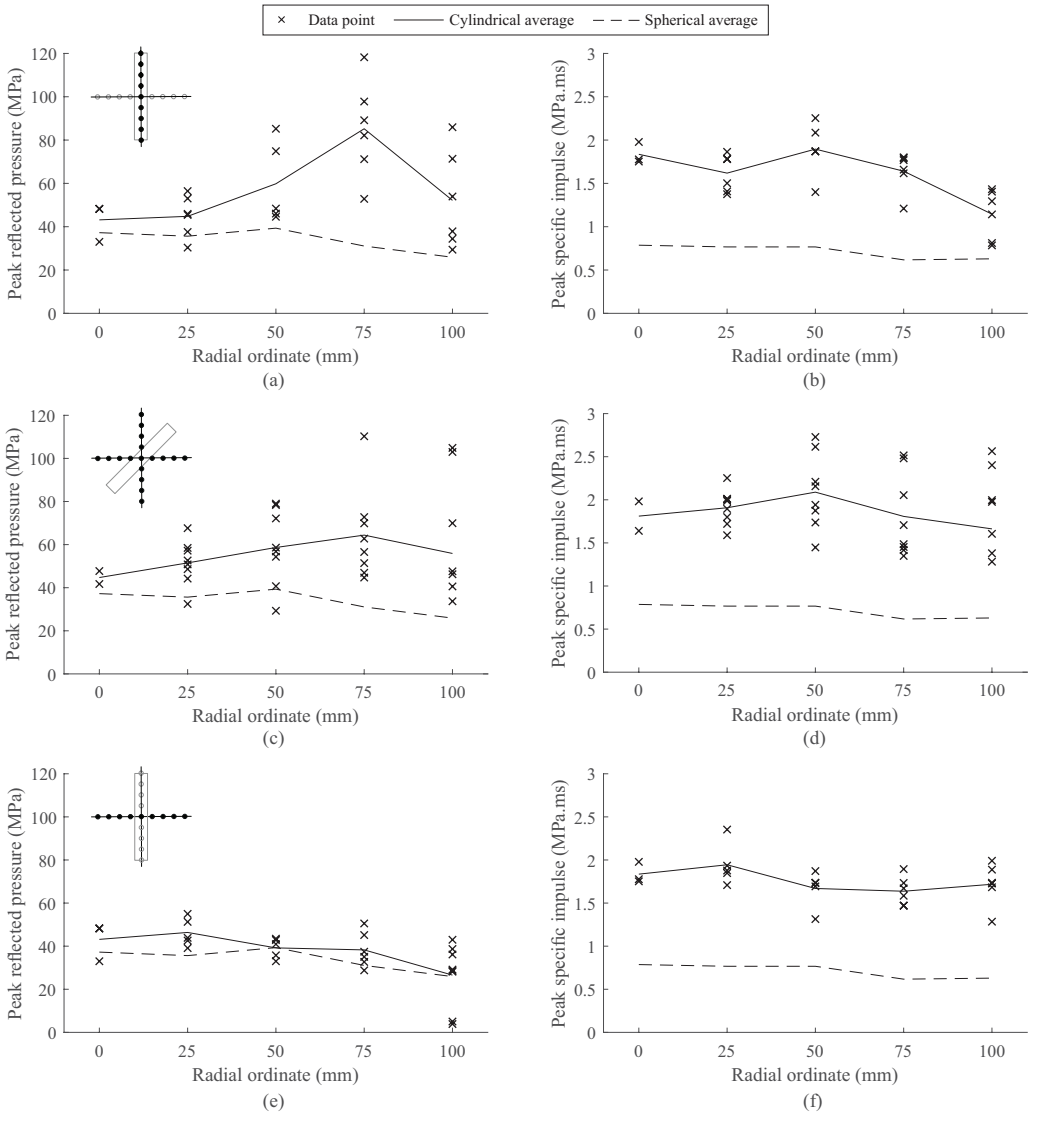

Figure 9. Compiled peak reflected pressure and peak specific impulse versus radial ordinate from detonation of 200 g $L/D = 7$ cylinders of C4 and 200 g spheres of C4 at 250 mm clear stand-off: (a–b) 0°, (c–d) 45° and (e–f) 90°.

The peak reflected pressures at 90° orientation generally follow the cylindrical peak pressure distributions, however the peak specific impulse is again approximately twice the spherical values. Whilst the specific impulse distribution at 0° appears to reduce with distance on account of the reduction of the 100 mm bar impulse due to localised clearing as explained previously, the 45° and 90° specific impulse distributions appear relatively uniform with radial ordinate.

Figure 10 shows quarter-symmetric surface plots of the distributed specific impulse from the spherical and cylindrical charges. Linear interpolation was used to map the mean specific impulse distributions from Figure 9 onto a regular Cartesian grid at 0.5 mm spacing. The spherical data

Table 3. Mean peak pressure and mean peak specific impulse at each radial ordinate for spheres and cylindrical charges at 0°, 45° and 90° orientation. Central bar data for Test 4 (spherical charge) omitted.

Radial ordinate (mm)	Peak pressure (MPa)				Peak specific impulse (MPa.ms)			
	Sphere	0°	45°	90°	Sphere	0°	45°	90°
0	37.2	41.2	44.7	41.2	0.79	1.56	1.81	1.56
25	35.6	44.6	51.5	48.4	0.77	1.59	1.91	1.75
50	39.3	59.5	58.7	39.2	0.77	1.81	2.09	1.59
75	31.1	79.2	66.1	41.9	0.62	1.62	1.81	1.48
100	25.9	45.9	63.7	34.4	0.63	1.06	1.89	1.58

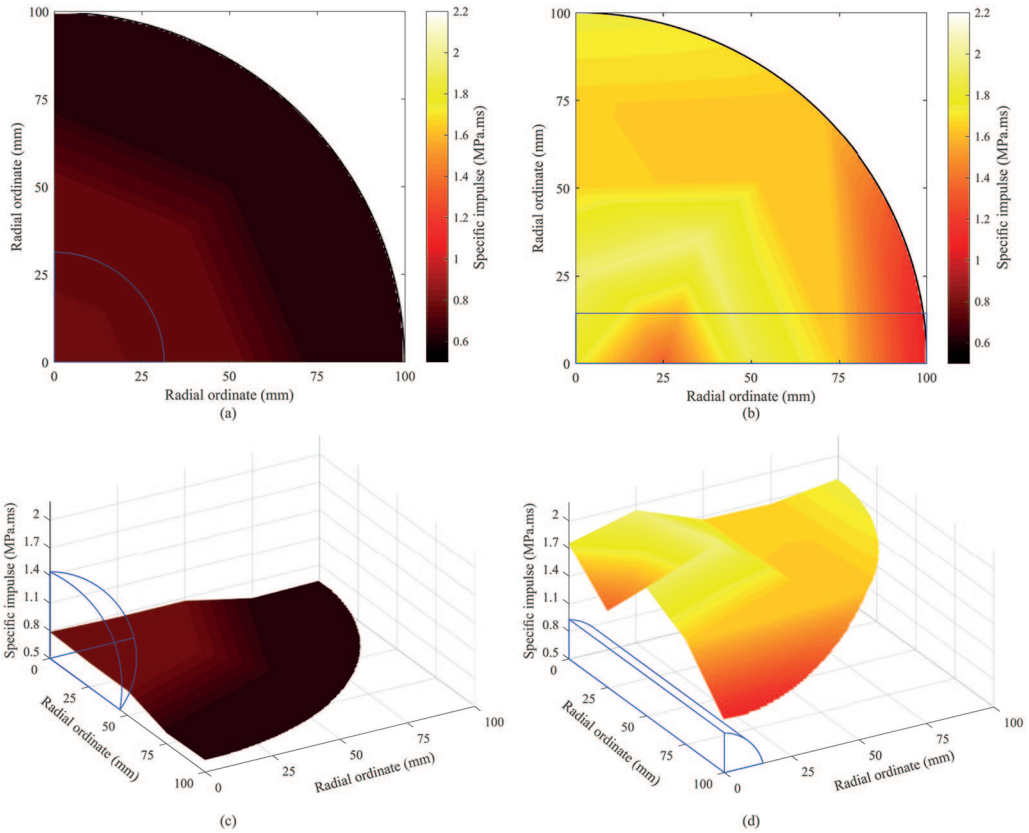

Figure 10. Interpolated peak specific impulse surface plots for spherical (a, c) and cylindrical (b, d) charges. Blue outline represents charge shape/orientation.

utilised 1D interpolation as a function of radial ordinate, whereas the cylindrical data required interpolation in 2D as a function of radial ordinate and orientation with respect to the longitudinal axis of the cylinder. Linear interpolation was used throughout, and is considered adequate here for illustrative purposes.

The enhancement provided by the cylindrical charges is immediately apparent, that is, the loading is less regular across the target face, it decays in a less consistent manner with radial ordinate,

Table 4. Relative standard deviation (RSD, %) of cylindrical charge peak pressure and peak specific impulse at 0°, 45° and 90° orientations. Row-wise and column-wise averages denote the mean RSD for a given radial ordinate and a given orientation respectively. RSD_{100}/RSD_{25} denotes the ratio between the RSDs at 100 mm and 25 mm radial ordinates for a given orientation.

Radial ordinate (mm)	Relative standard deviation (%)						Avg. (rows)
	Peak pressure			Peak specific impulse			
	0°	45°	90°	0°	45°	90°	
25	19.8	19.0	25.3	15.9	10.0	16.5	17.7
50	27.7	28.2	35.9	11.4	19.4	9.4	22.0
75	31.3	29.7	17.1	14.8	24.9	9.3	21.2
100	42.4	43.1	15.0	31.4	24.1	12.8	28.1
Avg. (cols)	30.3	30.0	23.3	18.4	19.6	12.0	–
RSD_{100}/RSD_{25}	2.1	2.3	0.6	2.0	2.4	0.8	–

and is considerably higher in magnitude throughout. These surface plots also provide a clear visualisation of the effects of the complex side, end, and bridging wave interaction phenomena occurring at approximately 50–75 mm from the centre of the cylinder as described previously. Finally, the rapid reduction in loading towards the end of the cylinder (100 mm radial ordinate at 0° orientation) is clearly visible.

Localised variability as a function of orientation and radial ordinate

From inspection of Figure 9, it is clear that the variations in near-field loading are considerably higher than the variations observed in the preliminary far-field testing (Figure 2), and the repeatability of near-field blast load measurement from cylindrical charges is dependent on both radial ordinate and orientation angle. For example, the range of peak reflected pressure at 75 mm and 0° orientation is approximately $\pm$ 35 MPa from the mean, whereas at the same radial ordinate at 90° orientation the deviation is approximately $\pm$ 10 MPa from the mean.

Table 4 shows the relative standard deviation (RSD, given as the standard deviation normalised by the mean value, expressed as a percentage) of the cylindrical charge peak pressure and peak specific impulse measurements. The RSDs are provided for each radial ordinate and orientation angle. The RSDs are calculated from six individual data points for the 0° and 90° orientation tests (two HPB arrays per test, three tests in total), and eight individual data points for the 45° tests (four HPB arrays per test, two tests in total). Central bar data have been omitted from the statistical analysis on account of the low number of data points per arrangement (three for 0° and 90° orientations, two for 45° orientation). Additionally, the average RSDs at a particular radial ordinate (row-wise mean) and orientation angle (column-wise mean) are also provided. Finally, the ratio between the RSD at 100 mm radial ordinate and the RSD at 25 mm radial ordinate is provided in order to make comments on how the variability increases with distance for a particular orientation.

Peak pressure RSDs are larger than peak specific impulse RSDs throughout. This indicates that complex features causing variability in the pressure histories, such as primary (side and end) and bridging wave interaction as described previously, has a lesser impact on the development of peak specific impulse. Higher variability in peak pressure measurements relative to variability in peak specific impulse measurements have also been observed in experiments quantifying the output from buried explosives (Rigby et al., 2016).

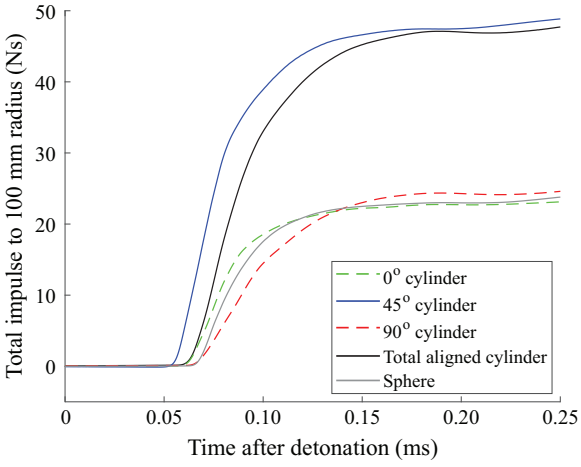

Figure 11. Temporal development of total impulse for spheres and cylinders. 45° cylinder loading integrated over the entire area, whereas 0° and 90° orientation loading integrated over half the swept area. These two combined give the 'Total aligned cylinder' trace.

The column-wise mean RSDs show that variability in loading at 0° and 45° orientation is higher than that at 90° orientation, for both pressure and impulse. It is suggested that the aforementioned side, end and bridging wave interaction is a localised feature that occurs near the ends of the cylinder, leaving the lateral expansion of the side wave (in the 90°, or perpendicular direction) relatively unaffected. This is further evidenced when considering the RSD_{100}/RSD_{25} values: at 0° and 45° orientation, the variability in loading at 100 mm radial ordinate is consistently a factor of two greater than the variability in loading at 25 mm. Conversely, at 90° orientation, the loading at 100 mm is less variable than the loading at 25 mm. This observation applies to both pressure and impulse.

The row-wise mean RSDs demonstrate a general-positive correlation between variability and radial ordinate, which suggests that the increasing variability at 0° and 45° orientation is dominant over the slight decrease in variability at 90° orientation. An increase in variability with radial ordinate is observed in tests with buried explosives (Rigby et al., 2016, 2018b).

Development of total impulse

Whilst specific impulse is a useful metric for both numerical model validation and assessing structural response, development of total impulse (specific impulse integrated with respect to area) is another key parameter as it signifies the total momentum imparted to a structure.

Figure 11 shows the temporal development of total impulse imparted to the central 200 mm diameter instrumented area of the target. Total impulse is calculated at each timestep using an area-weighted linear interpolation of the specific impulse distributions, sampled at 1 mm increments of radial ordinate. The spherical and 45° orientation loadings have been integrated over the entire instrumented area, whereas the 0° and 90° orientation loadings have each been integrated over half the swept area to separate total impulse into parallel and perpendicular components. 'Total aligned cylinder' is given by the summation of the parallel and perpendicular components of total impulse.

The staggered shock front arrival time along the 90° array results in a more gradual development of total impulse when compared to the 0° orientation loading, which demonstrates a sharper

rise on account of the concurrent shock front arrival times seen in Figure 8(a). Despite differences in the temporal development of total impulse, both components result in a similar final value which, when these two components are superimposed, results in a similar total impulse to the 45° loading. This suggests that, whilst there are clearly two distinct mechanisms governing load development along the parallel and perpendicular arrays, this results in notable differences in *specific* impulse distribution along a particular array but the development of *total* impulse appears invariant of charge orientation.

The total impulse imparted to the target following detonation of the cylindrical charges is over twice that imparted by the spherical charges, which follows the approximate factor of two difference seen in the specific impulse distributions, for example, Figures 9 and 10.

Numerical modelling

Numerical model setup

In this section, numerical analysis is used to qualitatively investigate three observations from the experimental results, namely:

1. Near-uniform arrival time of the shock front along the 0° array, as in Figure 8(a)
2. Non-central peak reflected pressures along the 0° array, as shown in the 75 mm bar trace in Figure 8(a) and more generally in Figure 9(a).
3. Increased variability in loading along the 0° array compared to the 90° array, see Table 4.

A numerical simulation was performed using the Multi-Material Eulerian/Arbitrary Lagrangian-Eulerian solver in LS-DYNA (Hallquist, 2006), following the methodology outlined in Langran-Wheeler et al. (2017, 2019). LS-DYNA has previously been validated against near-field spherical and cylindrical experimental data (Rigby et al., 2018c). Since the model here is intended to investigate the emergence and development of features within the expanding shock front, it is only necessary to model incident conditions and therefore the problem can be represented in 2D axi-symmetry.

A domain of 0.4 m by 0.8 m was discretised into 0.5 mm square, volume-weighted 2D axi-symmetric elements, with the element size informed by previous mesh convergence studies (Langran-Wheeler et al., 2017, 2019). The domain was initially filled with air, modelled using the *MAT_NULL material model and linear polynomial equation of state (EOS), *EOS_LINEAR_POLYNOMIAL:

$$p = C_0 + C_1\mu + C_2\mu^2 + C_3\mu^3 + (C_4 + C_5\mu + C_6\mu^2)E \tag{1}$$

where $C_0, C_1, C_2, C_3, C_4, C_5, C_6$ are constants, $\mu = \rho / \rho_0 - 1$, ρ and ρ_0 are the current and initial densities of air respectively, and E is the specific internal energy. The ideal gas equation of state was recovered by setting $C_0 = C_1 = C_2 = C_3 = C_6 = 0$, and $C_4 = C_5 = \gamma - 1$, where $\gamma = 1.4$ is the ratio of specific heats for air:

$$p = (\gamma - 1)E\rho / \rho_0 \tag{2}$$

The initial specific internal energy was set as $E_0 = 253.4$ kPa to give an atmospheric pressure of 101.4 kPa. The explosive geometry was represented using *INITIAL_VOLUME_FRACTION_GEOMETRY by specifying a 200 mm long, 14.3 mm high rectangle, centred on the axis, which would represent a 28.6 mm diameter cylinder when rotated about the axis. The C4 explosive was

Table 5. Material model and equation of state parameters for air and C4, taken from Dobratz and Crawford (1985).

*MAT_NULL			*MAT_HIGH_EXPLOSIVE_BURN		
Parameter	Value	Unit	Parameter	Value	Unit
ρ_0	1.225	kg/m^3	ρ_0	1601	kg/m^3
			D	8193	m/s
			P_{CJ}	28.00e9	Pa
*EOS_LINEAR_POLYNOMIAL			*EOS_JWL		
Parameter	Value	Unit	Parameter	Value	Unit
C_0	0.0	Pa	A	609.77e9	Pa
C_1	0.0	Pa	B	12.95e9	Pa
C_2	0.0	Pa	R_1	4.50	–
C_3	0.0	Pa	R_2	1.40	–
C_4	0.4	–	ω	0.25	–
C_5	0.4	–	E_0	9.00e9	Pa
C_6	0.0	–			
E_0	253.40e3	Pa			

modelled using the Jones-Wilkins-Lee (JWL) semi-empirical equation of state, *EOS_JWL (Lee et al., 1968):

$$p = A\left(1-\frac{\omega}{R_1 V}\right)e^{-R_1 V} + B\left(1-\frac{\omega}{R_2 V}\right)e^{-R_2 V} + \frac{\omega E}{V} \tag{3}$$

where A, B, R_1, R_2 and ω are constants, V is the volume and E is the specific internal energy as before.

Density, ρ, detonation velocity, D and Chapman-Jouguet pressure, P_{CJ}, of the explosive are defined in the *MAT_HIGH_EXPLOSIVE_BURN material model and control the programmed detonation of the explosive. Material properties and EOS parameters used in the numerical model are summarised in Table 5, where the JWL parameters for C4 are taken from Dobratz and Crawford (1985).

In this configuration, the 0° array is given by a line parallel to the symmetry axis, 264.3 mm from the charge centre. Whilst the 90° array is out-of-plane in the 2D model, its effective position can be mapped onto the 2D domain as a series of in-plane points, each with equal distance to the charge centre as the corresponding points in the 90° array. For example, the 100 mm bar in the 90° array is a total slant distance of $\sqrt{(264.3^2 + 100^2)} = 282.6$ mm from the centre of the charge (where 264.3 mm is the normal stand-off distance and 100 mm is the lateral distance along the target). The general geometry of the numerical model is represented in the first image in Figure 12, with representative bar locations indicated by 'x' and 'o' markers for 0° and 90° arrays respectively. The axis of symmetry is also labelled, and the indicative position of the target plate is given as a horizontal line.

Numerical model results

Figure 12 shows fringe plots of material volume fraction (1.0 represents pure explosive detonation products and 0.0 represents pure air), incident pressure, and resultant acceleration, which is analogous to the pressure gradient (Rigby et al., 2014b).

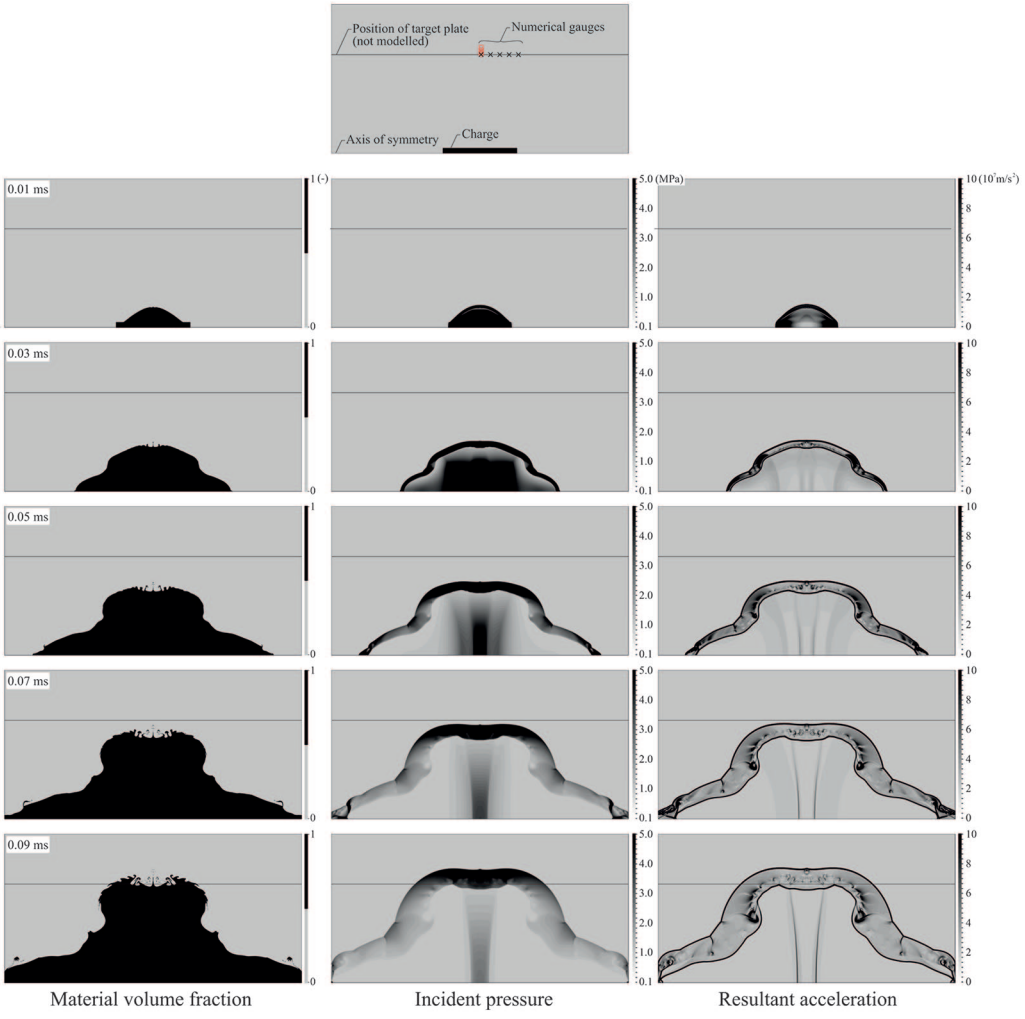

Figure 12. Fringe plots of volume fraction material (explosive detonation products), incident pressure and resultant acceleration from detonation of 200 g $L/D = 7$ cylinders of C4 modelled. Representative bar locations are indicated by 'x' and 'o' markers for 0° and 90° arrays respectively. Note that target position is for indication only; an incident analysis was performed and the target itself was not explicitly modelled.

When considering the material volume fraction plots, at 0.01 ms, the detonation products have begun expanding in the radial direction whilst the detonation wave is still some distance from the axial end of the explosive, causing the detonation product breakout to be initially spherical in shape. As time progresses, the detonation products become increasingly prolate, until at approximately 0.05 ms after detonation when the explosive products become flat-topped with respect to the target plate. This continues until the detonation products and shock waves impinge on the target plate, which would occur between 0.07 and 0.09 ms had the problem not been modelled in axi-symmetry.

Numerical arrival times have been evaluated by taking the time at which the first non-zero pressure was recorded along an array of tracer particles representing the 0° and 90° arrays. Figure 13 shows a comparison of these numerical arrival times with the experimentally-recorded arrival

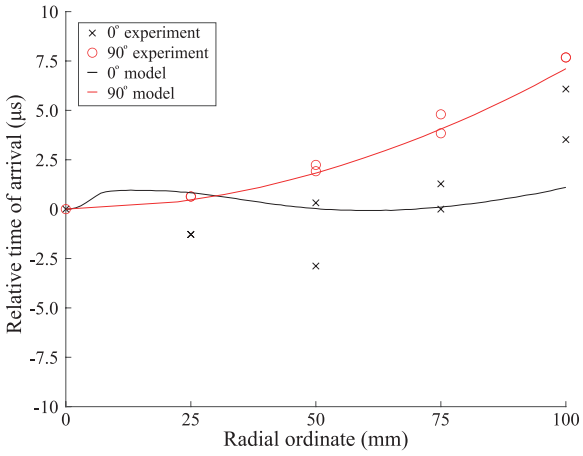

Figure 13. Relative time of arrival of the blast wave at radial ordinates for 0° and 90° arrays: numerical results (incident) compared against recorded arrival times in Test 7.

times from Test 7. Here, the results are presented as relative arrival time, that is, with the arrival time at the central bar subtracted, for ease of comparison between the two. It can be clearly seen that arrival times along the 0° array are reasonably consistent, whereas arrival times along the 90° increase with increasing radial ordinate. Numerical and experimental results are in good agreement, with a maximum variation of 5 μs between the numerical and experimental relative arrival times. It can be said with some confidence, therefore, that observation 1 above is as a result of the flat-topped nature of the expanding detonation product cloud.

With reference to the pressure plots in Figure 12, the initial expansion of the shock front appears to be effectively spherical in nature. However, as the detonation wave progresses along the axis of the charge, more material becomes available to confine the expanding detonation products, and the shock front is subjected to increasing levels of lateral inertial confinement, as observed in Nurick et al. (2016). Hence, as the shock front continues to expand (i.e. between 0.05 and 0.07 ms), the highest pressures are not located directly in the centre of the detonation product cloud, but some position off-centre. The numerical and experimental results show that, for this geometry, the peak pressure acts on the target approximately 75 mm from the centre (observation 2 above). The indicative modelling suggests that this is due to inertial self-confinement of the detonation products.

Finally, the resultant acceleration plots in Figure 12 reveal complex structures in the region between the shock front and detonation products. These are particularly prominent at later times, and are focussed around the region where the detonation products transition from flat-topped to rounded (approximately 75–100 mm from the charge centre for this geometry). These structures are evidence of complex interactions between the primary end waves and bridging waves, and give rise to more complex and variable behaviour at the remote bar locations, thereby supporting observation 3 above.

Summary and conclusions

This paper presents the experimental results characterising near-field blast loading from 200 g spheres and horizontally-aligned 200 g cylinders ($L / D = 7$, longitudinal axis parallel to the span of the target) of C4 bare HE charges placed at 250 mm clear stand-off from a rigid target. Two

cylindrical configurations were tested: one series of experiments were conducted with the cylinders orientated parallel and perpendicular to the two measurement arrays (enabling separation of the 0° and 90° components of loading, that is, orientated with and parallel to the longitudinal axis of the charge respectively), and one series of the experiments with the longitudinal axis of the charge orientated at 45° to the measurement arrays.

A preliminary series of far-field testing indicated a high level of repeatability of far-field loading parameters. The near-field cylindrical results were then compared with the spherical data in terms of pressure histories at a given position on the target, distribution of peak pressure and peak specific impulse with distance from the target, and development of total impulse. Variability in cylindrical loading parameters was also investigated.

The results showed that the parallel component of loading is characterised by uniform arrival times, a sharp rise to peak pressure and more rapid decay to ambient pressure, with a sharp drop-off in loading beyond the ends of the cylinder. The perpendicular component of loading is characterised by staggered arrival times, a more gradual rise to peak pressure and a prolonged decay to ambient pressure thereafter. Charge orientation was shown to influence the spatial and temporal development of pressure, but not total impulse. Furthermore, peak pressure and peak specific impulse along the parallel array were considerably more variable and complex than those along the perpendicular array, attributed to complex wave interactions formed by coalescence of the primary waves from the radial ('side') and axial faces ('end') of the charge, and the bridging wave between the two. Indicative numerical modelling was used to qualitatively confirm the presence of these features.

Significant differences were observed between the loading from the cylindrical and spherical charges. The cylindrical charge imparted loading that was less regular across the target face, decaying in a less consistent manner (with increasing distance from the plate centre), and was considerably higher in magnitude throughout, by approximately a factor of two.

Assessment of structures subjected to near-field blast, and the provision of adequate protective systems, requires a comprehensive understanding of the mechanisms and magnitude of load development on the target face. Detailed experimental studies, such as those presented in this article, enable for accurate quantification of the highly complex loading acting on a reflecting surface following detonation of a close-in, non-spherical explosive, and can be used as a benchmark for future numerical modelling studies and additional experimental work.

Declaration of conflicting interests

The author(s) declared no potential conflicts of interest with respect to the research, authorship, and/or publication of this article.

Funding

The author(s) disclosed receipt of the following financial support for the research, authorship, and/or publication of this article: The first author acknowledges financial support provided by the U.S. Army Engineer Research and Development Center W9132T-16-2-0015. A. Tyas would like to express his gratitude to the Royal Academy of Engineering and the Defence Science and Technology Laboratory for funding his position as RAEng/Dstl Research Professor of Blast Engineering.

ORCID iD

Sam Rigby https://orcid.org/0000-0001-6844-3797

References

Artero-Guerrero J, Pernas-Sánchez J and Teixeira-Dias F (2017) Blast wave dynamics: The influence of the shape of the explosive. *Journal of Hazardous Materials* 331: 189–199.

Bogosian D, Yokota M and Rigby S (2016) TNT equivalence of C-4 and PE4: A review of traditional sources and recent data. In: *Proceedings of the 24th international symposium on Military Aspects of Blast and Shock (MABS24)*, Halifax, Nova Scotia, Canada, 19–23 September.

Clarke SD, Fay SD, Warren JA, et al. (2015) A large scale experimental approach to the measurement of spatially and temporally localised loading from the detonation of shallow-buried explosives. *Measurement Science and Technology* 26: 015001.

Cranz C (1926) *Lehrbuch der Basllistik*. Berlin: Springer.

Dobratz P and Crawford B (1985) LLNL explosives handbook – properties of chemical explosives and explosive simulants. Technical report, Lawrence Livermore National Laboratory, CA.

Esparza ED (1992) Spherical equivalency of cylindrical charges in free-air. In: *25th Department of defense explosives safety seminar*, Anaheim, CA, 18–20 August.

Fay S, Clarke S, Warren JA, et al. (2013) Capturing the spatial and temporal variations in impulse from shallow buried charges. In: *Proceedings of the 15th international symposium on the interaction of the effects of munitions with structures (ISIEMS15)*, Potsdam, Germany, 17–20 September.

Friedlander FG (1946) The diffraction of sound pulses. I. Diffraction by a semi-infinite plane. *Proceedings of the Royal Society A: Mathematical, Physical and Engineering Sciences* 186(1006): 322–344.

Hallquist JO (2006) *LS-DYNA Theory Manual*. Livermore, CA: Livermore Software Technology Corporation.

Hopkinson B (1914) A method of measuring the pressure produced in the detonation of high explosives or by the impact of bullets. *Philosophical Transactions of the Royal Society of London. Series A, Containing Papers of a Mathematical or Physical Character* 213(497–508): 437–456.

Hopkinson B (1915) British ordnance board minutes. Report 13565, British Ordnance Office, London.

Hu Y, Chen L, Fang Q, et al. (2018) Blast loading model of the RC column under close-in explosion induced by the double-end-initiation explosive cylinder. *Engineering Structures* 175: 304–321.

Hyde DW (1991) *Conventional Weapons Effect Program (ConWep)*. U.S Army Waterways Experimental Station, Vicksburg, MS.

Kingery CN and Bulmash G (1984) Airblast parameters from TNT spherical air burst and hemispherical surface burst. Report ARBRL-TR-02555, US Army Ballistic Research Laboratory, Aberdeen Proving Ground, MD.

Knock C and Davies N (2011a) Predicting the impulse from the curved surface of detonating cylindrical charges. *Propellants, Explosives, Pyrotechnics* 36(2): 105–109.

Knock C and Davies N (2011b) Predicting the peak pressure from the curved surface of detonating cylindrical charges. *Propellants, Explosives, Pyrotechnics* 36(3): 203–209.

Knock C and Davies N (2013) Blast waves from cylindrical charges. *Shock Waves* 23(4): 337–343.

Knock C, Davies N and Reeves T (2015) Predicting blast waves from the axial direction of a cylindrical charge. *Propellants, Explosives, Pyrotechnics* 40(2): 169–179.

Langran-Wheeler C, Tyas A, Rigby S, et al. (2017) Characterisation of reflected blast loads in the very-near field from non-spherical explosive charges. In: *Proceedings of the 17th international symposium for the interaction of munitions with structures (ISIEMS17)*, 16 October, Bad Neuenahr, Germany.

Langran-Wheeler C, Tyas A, Rigby S, et al. (2019) Reflected blast loads from long cylinders in the near-field. In: *Proceedings of the 18th international symposium for the interaction of munitions with structures (ISIEMS18)*, Panama City, FL.

Lee EL, Hornig HC and Kury JW (1968) Adiabatic expansion of high explosive detonation products. Technical report TID 4500-UCRL 50422, Lawrence Radiation Laboratory, University of California, CA.

Lord Rayleigh (1882) Investigation of the character of the equilibrium of an incompressible heavy fluid of variable density. *Proceedings of the London Mathematical Society* 4(1): 170–177.

Meshkov EE (1969) Instability of the interface of two gases accelerated by a shock wave. *Fluid Dynamics* 4: 101–104.

Nurick GN, Mahoi S and Langdon GS (2016) The response of plates subjected to loading arising from the detonation of different shapes of plastic explosive. *International Journal of Impact Engineering* 89: 102–113.

Plooster MN (1978) Blast front pressure from cylindrical charges of high explosives. TM 3631, Naval Weapons Center, Denver Research Institute, China Lake, CA.

Plooster MN (1982) Blast effects from cylindrical explosive charges: Experimental measurements. NWC TP 6382, Naval Weapons Center, Denver Research Institute, China Lake, CA.

Richtmyer RD (1960) Taylor instability in a shock acceleration of compressible fluids. *Communications on Pure and Applied Mathematics* 13: 297–319.

Rigby SE, Akintaro OI, Fuller BJ, et al. (2019a) Predicting the response of plates subjected to near-field explosions using an energy equivalent impulse. *International Journal of Impact Engineering* 128: 24–36.

Rigby SE, Barr A and Clayton M (2018a) A review of Pochhammer-Chree dispersion in the Hopkinson bar. *Proceedings of the Institution of Civil Engineers: Engineering and Computational Mechanics* 171(1): 3–13.

Rigby SE, Fay SD, Clarke S, et al. (2016) Measuring spatial pressure distribution from explosives buried in dry Leighton Buzzard sand. *International Journal of Impact Engineering* 96: 89–104.

Rigby SE, Fay SD, Tyas A, et al. (2018b) Influence of particle size distribution on the blast pressure profile from explosives buried in saturated soils. *Shock Waves* 28(3): 613–626.

Rigby SE, Fay SD, Tyas A, et al. (2015a) Angle of incidence effects on far-field positive and negative phase blast parameters. *International Journal of Protective Structures* 6(1): 23–42.

Rigby SE, Fuller BJ and Tyas A (2018c) Validation of near-field blast loading in LS-DYNA. In: *Proceedings of the 5th international conference on protective structures (ICPS5)*, Poznan, Poland, August 20–24.

Rigby SE and Gitterman Y (2016) Secondary shock delay measurements from explosive trials. In: *Proceedings of the 24th international symposium on military aspects of blast and shock (MABS24)*, Halifax, Nova Scotia, Canada, 19–23 September.

Rigby SE, Knighton R, Clarke SD, et al. (2020) Reflected near-field blast pressure measurements using high speed video. *Experimental Mechanics* 60(7): 875–888.

Rigby SE, Osborne C, Langdon GS, et al. (2021) Spherical equivalence of cylindrical explosives: Effect of charge shape on deflection of blast-loaded plates. *International Journal of Impact Engineering*. DOI: https://doi.org/10.1016/j.ijimpeng.2021.103892.

Rigby SE, Tyas A, Bennett T, et al. (2014a) The negative phase of the blast load. *International Journal of Protective Structures* 5(1): 1–20.

Rigby SE, Tyas A, Bennett T, et al. (2014b) A numerical investigation of blast loading and clearing on small targets. *International Journal of Protective Structures* 5(3): 253–274.

Rigby SE, Tyas A, Clarke SD, et al. (2015b) Observations from preliminary experiments on spatial and temporal pressure measurements from near-field free air explosions. *International Journal of Protective Structures* 6(2): 175–190.

Rigby SE, Tyas A, Curry RJ, et al. (2019b) Experimental measurement of specific impulse distribution and transient deformation of plates subjected to near-field explosive blasts. *Experimental Mechanics* 59(2): 163–178.

Rigby SE, Tyas A, Fay SD, et al. (2014c) Validation of semi-empirical blast pressure predictions for far field explosions – is there inherent variability in blast wave parameters? In: *6th International conference on protection of structures against hazards (PSH14)*, Tianjin, China, 16–17 October.

Sherkar P, Shin J, Whittaker A, et al. (2016) Influence of charge shape and point of detonation on blast-resistant design. *Journal of Structural Engineering* 142(2): 04015109.

Shi Y and Stewart G (2015) Damage and risk assessment for reinforced concrete wall panels subjected to explosive blast loading. *International Journal of Impact Engineering* 85: 5–19.

Simoens B and Lefebvre M (2015) Influence of the shape of an explosive charge: Quantification of the modification of the pressure field. *Central European Journal of Energetic Materials* 12: 195–213.

Stoner RG and Bleakney W (1948) The attenuation of spherical shock waves in air. *Journal of Applied Physics* 19(7): 670–678.

Swizdak MM (1982) *Explosion effects and properties, part 1 – explosion effects in air*. Report NSWC/WOL/TR 75-116, Naval Surface Weapons Report, White Oak, MD.

Taylor GI (1950) The instability of liquid surfaces when accelerated in a direction perpendicular to their planes. I. *Proceedings of the Royal Society A: Mathematical, Physical and Engineering Sciences* 201(1065): 192–196.

Tyas A (2019) Blast loading from high explosive detonation: What we know and what we don't know. In: *13th International conference on shock and impact loads on structures*, Guangzhou, China, 13–15 December.

Tyas A, Reay JJ, Fay SD, et al. (2016) Experimental studies of the effect of rapid afterburn on shock development of near-field explosions. *International Journal of Protective Structures* 7(3): 456–465.

Tyas A, Warren J, Bennett T, et al. (2011) Prediction of clearing effects in far-field blast loading of finite targets. *Shock Waves* 21(2): 111–119.

Tyas A and Watson AJ (2001) An investigation of frequency domain dispersion correction of pressure bar signals. *International Journal of Impact Engineering* 25(1): 87–101.

US Department of Defence (2008) Structures to resist the effects of accidental explosions. UFC 3-340-02, US DoD, Washington, DC.

Wisotski J and Snyer WH (1965) Characteristics of blast waves obtained from cylindrical high explosive charges. Report, University of Denver, Denver Research Institute, CO.

Wu C, Fattori G, Whittaker A, et al. (2010) Investigation of air-blast effects from spherical-and cylindrical-shaped charges. *International Journal of Protective Structures* 1(3): 345–362.

Xiao W, Andrae M and Gebbeken N (2020a) Effect of charge shape and initiation configuration of explosive cylinders detonating in free air on blast-resistant design. *Journal of Structural Engineering* 146(8): 04020146.

Xiao W, Andrae M and Gebbeken N (2020b) Influence of charge shape and point of detonation of high explosive cylinders detonated on ground surface on blast-resistant design. *International Journal of Mechanical Sciences* 181: 105697.